ChemElectroChem

Research Article
doi.org/10.1002/celc.202200825

Chemistry Europe
European Chemical Societies Publishing

www.chemelectrochem.org

Special Collection

Lithium Dependent Electrochemistry of p-Type Nanocrystalline $CuCrO_2$ Films

Amanda L. Chown,[a] Humaira Yeasmin,[a] Rajendra Paudel,[b] Ryan B. Comes,[b] and Byron H. Farnum*[a]

$CuCrO_2$ nanocrystals were synthesized and fabricated into mesoporous thin films to study their electrochemical properties, where a strong [Li^+] dependence was observed. An anodic shift in the $Cu^{2+/+}$ redox potential was observed with increased [Li^+] in the electrolyte, in addition to the growth of a new redox feature at $E_{1/2} = -0.43$ V vs $Fc^{+/0}$. This new feature was attributed to $Cu^{2+/+}$ redox chemistry accompanied by Li^+ occupation in copper vacancy surface defects. The equilibrium constant and maximum charge for Li^+ occupation were determined to be $K = 0.057\ M^{-1}$ and 15.5 mC, respectively. The maximum charge was close to the expected value of 11 mC based on the measured concentration of copper vacancies. The pronounced Li^+ dependent electrochemistry suggests that $CuCrO_2$ behaves similarly to cathodes in Li-ion batteries. Thus, chronopotentiometry experiments revealed a $7.8\ mA\,h\,g^{-1}$ charge capacity at cycle 2 and increasing cycling efficiency from 83 to 91% over 10 cycles. However, a pronounced decrease in charge capacity was observed with increased cycles, attributed to a loss in lithium-coupled electrochemistry. These studies add to our understanding of surface defects in p-type oxides and their effect on hole recombination in solar cell devices.

Introduction

N-type and p-type metal oxides have found great use as selective contacts in a variety of heterojunction solar cell architectures including dye-sensitized solar cells, quantum dot solar cells, organic photovoltaics, and perovskite solar cells.[1–6] N-type materials such as TiO_2, SnO_2, and ZnO are used to selectively move electrons from light absorbers to the external circuit.[7–11] Likewise, p-type materials such as NiO and $CuMO_2$ ($M = Cr^{3+}$, Ga^{3+}) are used to accept and transport holes from light absorbers to the external circuit.[12,13] Given the interfacial relationship between the metal oxide and light absorbers required for charge transfer, a fundamental understanding of the band structure and surface electronic states of these materials is important. The electrochemical features which describe band edges and surface states for n-type oxides TiO_2, SnO_2, and ZnO and p-type NiO have been well studied in the literature;[1–3,7,8] however, only a handful of studies have presented such data for $CuMO_2$ materials.[14–19] Further understanding of the electrochemical behavior of $CuMO_2$ oxides could provide insight into how to fully utilize them in solar cell architectures.

$CuMO_2$ oxides are a variable class of materials with a wide range of M^{3+} cations able to be incorporated. $CuCrO_2$ and $CuGaO_2$ have become popular choices for p-type hole transport materials for solar cells due to their wide direct band gaps, 3.3 and 3.6 eV, respectively.[14,20] The delafossite crystal structure (Figure 1) of these materials lends itself to hole transport through the Cu^+ sheets sandwiched between edge-shared $M^{3+}O_6$ octahedra. This layered structure in turn results in hexagonal plate-like nanocrystal morphologies with anisotropic hole transport. For example, the diffusion coefficient parallel to the Cu^+

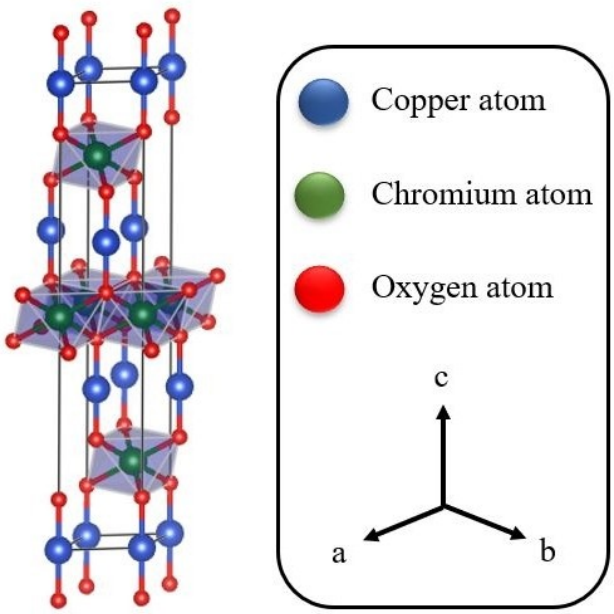

Figure 1. Delafossite unit cell for $CuCrO_2$ in 3R phase.

[a] A. L. Chown, H. Yeasmin, Prof. B. H. Farnum
Department of Chemistry and Biochemistry
Auburn University
Auburn, AL 36849, United States
E-mail: farnum@auburn.edu
[b] R. Paudel, Prof. R. B. Comes
Department of Physics
Auburn University
Auburn, AL 36849, United States

Supporting information for this article is available on the WWW under https://doi.org/10.1002/celc.202200825

Special Collection An invited contribution to the Electrochemical Solar Energy Conversion and Storage Special Collection

plane has been measured to be ~25× larger than the diffusion coefficient perpendicular to the plane for $CuAlO_2$.[21]

The band structure of copper delafossite materials has been thoroughly investigated by theoretical means to conclude that the valence band contains a mixture of copper based 3d-orbitals and oxygen based 2p-orbitals.[22,23] Electrochemical determination of the valence band edges of $CuCrO_2$ and $CuGaO_2$ have been determined from Mott-Schottky measurements to be 0.8 V and 0.6 V vs NHE in 0.1 M Na_2HPO_4 electrolyte solution.[14,24,25] In the case of $CuGaO_2$, the valence band edge aligns well with a quasireversible feature observed with cyclic voltammetry and assigned to a $Cu^{2+/+}$ surface redox state induced by copper vacancy defects.[26] Similar surface defects have been described for p-type NiO, which also shares a similar band structure involving overlap of transition metal 3d-orbitals and oxygen 2p-orbitals.[27] The impact of these surface defects on the performance of dye-sensitized solar cells has also been of great interest in the literature as they can act as recombination centers with reduced dye molecules and redox mediators.[27] Numerous studies have shown that passivation of these states using targeted atomic deposition to fill nickel vacancies with redox inert M^{3+} cations in the lattice or atomic layer deposition of nanometer thick redox inert oxide materials (*e.g.* Al_2O_3) results in larger photovoltages but decreased photocurrent.[27–29]

Given the layered delafossite structure of $CuMO_2$ materials and the hexagonal plate-like morphology of nanocrystals, it is important to consider that copper-based charge transfer through either surface defect states or valence band states should be more favored along the "sides" of the nanocrystal where copper atoms terminate the lattice as opposed to the "top and bottom" where M^{3+} cations form a close-packed layer of edge-shared octahedra. Changes in aspect ratio of the nanocrystals may therefore impact the magnitude of the surface defect sites and/or the propensity of the material to perform charge transfer with light absorbing molecules and materials.

Here, we describe the electrochemical features of $CuCrO_2$ nanocrystals deposited as thin film electrodes on conductive glass. The preparation of $CuCrO_2$ and generation of the electrodes is designed to be consistent with how these materials would be used in heterojunction solar cells, particularly within dye-sensitized architectures. All experiments were performed with redox-inert electrolyte without the presence of light absorbing molecules so that the electrochemistry of the $CuCrO_2$ surface and valence band could be measured directly. Using a combination of electrochemical and spectroscopic methods, we show that quasi-reversible redox features at the electrode surface are consistent with $Cu^{2+/+}$ surface defects which are further activated by the presence of Li^+ in the electrolyte. The impact of these findings on the use of $CuCrO_2$ in heterojunction solar cells and electrochemical energy storage is further discussed.

Results and discussion

$CuCrO_2$ nanocrystals were synthesized following a previously published procedure from our group.[30] Solid material produced from that study were further used for experiments reported here, thus some characterization methods have been previously reported. Powder diffractograms are shown in Figure 2a for the synthesized $CuCrO_2$ nanocrystals after washing in 0.5 M NH_4OH for 24 hours. Distinct peaks are present at 31.0°, 36.2°, and 61.7° characteristic of the (006), (012), and (110) peaks, respectively for delafossite $CuCrO_2$ in the 3R phase (PDF #00-039-0247). The broad nature of the diffraction peaks was consistent with nanocrystalline particle sizes as observed in TEM images (Fig-

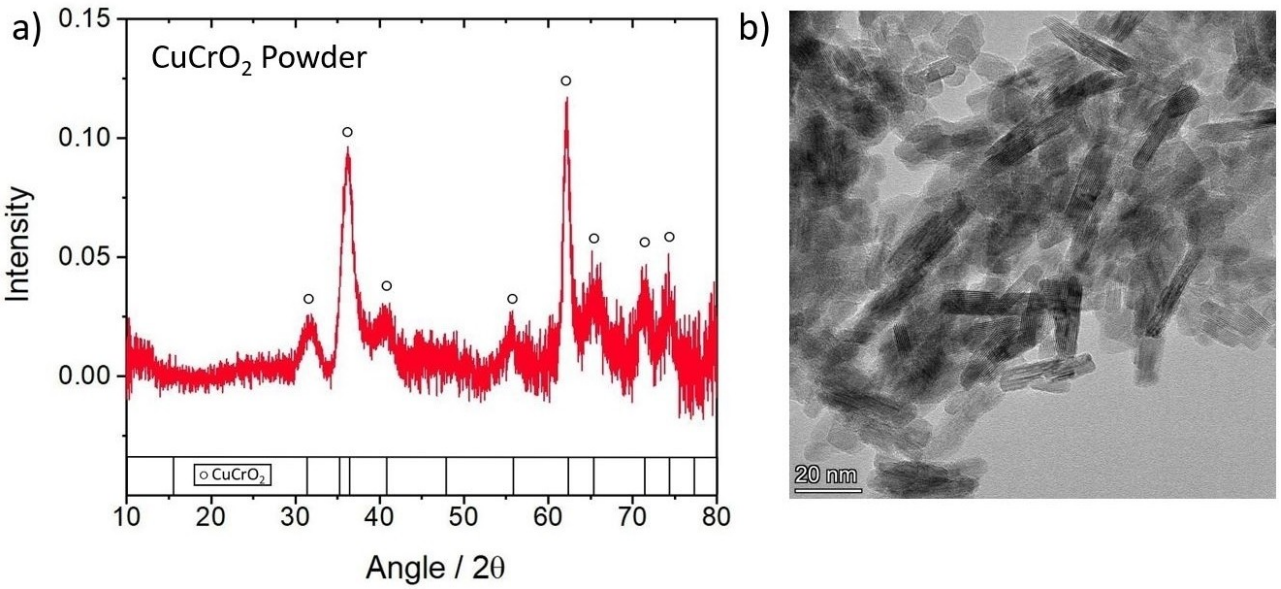

Figure 2. a) Powder X-ray diffractogram of synthesized $CuCrO_2$ powder. A standard diffraction pattern for $CuCrO_2$ (PDF #00-039-0247) is shown for comparison. b) TEM image of $CuCrO_2$ nanocrystals.

ure 2b). The anisotropic nanocrystals measured 22.9 ± 5.5 nm in width and 5.0 ± 1.7 nm in thickness, resulting in an aspect ratio of 4.6 ± 1.9. As previously reported, elemental analysis using ICP-MS found a 4.0 ± 1.5 at% deficiency in copper atoms compared with chromium, indicating the possible presence of copper vacancy defects.[30,32]

$CuCrO_2$ nanocrystals were mixed with ethyl cellulose and ethanol to form a viscous paste and dispersed onto conductive FTO glass using a spin coater to result in thin films of 1.43 ± 0.20 μm thickness. Films were then annealed at 350 °C to remove ethyl cellulose. Figure S1 shows powder diffractograms collected pre- and post-annealing to confirm the integrity of the $CuCrO_2$ solid. XPS studies on post-annealed $CuCrO_2$ films also supported the conclusion that Cu^{2+} sites are present to charge compensate for Cu^+ vacancies seen from ICP results, as previously reported.[30] Figure S2 shows Cu XPS spectra where the Cu region indicates a peak at 936.7 eV assigned to Cu^{2+}. Cr and O XPS data are also shown in addition to the survey scan.

Post-annealed $CuCrO_2$ films deposited on FTO glass were used directly as working electrodes in three-electrode electrochemical cells. Figure 3a shows cyclic voltammograms collected at 10 mV/s for $CuCrO_2$ electrodes in MeCN solution with different electrolytes. The potential was cycled three times where the data shown in Figure 3a represents the third cycle. All three cycles are shown in Figure S3. The total ionic strength for each electrolyte was fixed at 0.1 M for all experiments, but the amount of $LiClO_4$ and $TBAClO_4$ were varied to adjust the concentration of $[Li^+]$. Starting at 0 M $[Li^+]$ (*i.e.* 0.1 M $TBAClO_4$), the observed anodic and cathodic currents were relatively low with small peaks at $E_{pa} = 0.18$ and $E_{pc} = -0.13$ V vs $Fc^{+/0}$, yielding an $E_{1/2} = 0.03$ V. A much larger anodic feature was observed to begin around 0.5 V which was found to be consistent across all $[Li^+]$ electrolyte conditions. As Li^+ was introduced into the electrolyte, the E_{pa} and E_{pc} values appeared to shift positively to 0.24 and 0.03 V, respectively, at 0.1 M $[Li^+]$ with an $E_{1/2} = 0.14$ V. In addition, a new quasi-reversible redox feature was observed to increase in anodic current with an increase in $[Li^+]$ centered at $E_{1/2} = -0.43$ V ($E_{pa} = -0.05$ V, $E_{pc} = -0.81$ V) for 0.1 M $LiClO_4$. The cathodic peak for this new feature shifted positively from potentials less than −1.5 V to the final peak position of −0.8 V as $[Li^+]$ increased. It is important to note that the Cu^+ oxidation feature seen at 0.18 V vs $Fc^{+/0}$ is not seen if the potential window is reduced such that the cathodic potential ends at −0.4 V, as shown in the corresponding cyclic voltammograms in Figure S4.

Similar studies on $CuGaO_2$ nanocrystalline films in MeCN with 0.1 M $LiClO_4$ have reported a quasi-reversible redox feature with $E_{1/2} = 0.1$ V vs $Fc^{+/0}$, assigned to a $Cu^{2+/+}$ redox couple.[26] Given that these studies were performed at much higher scan rates and without a comparison to 0 M $[Li^+]$, we synthesized $CuGaO_2$ according to this previous report and generated comparable nanocrystalline films for electrochemical measurements. Figure 3b shows an overlay of the two materials, $CuCrO_2$ and $CuGaO_2$, in MeCN with 0.1 M $LiClO_4$ electrolyte. The current observed for $CuCrO_2$ greatly outweighs that observed for $CuGaO_2$. Some of this difference in current can be accounted for by the greater internal surface area observed for $CuCrO_2$ films (345 ± 63 cm^2) than for $CuGaO_2$ films (162 ± 25 cm^2), Table S1–2. However, this would represent only a ~2-fold increase in current for $CuCrO_2$ based on surface area, instead of the ~50-fold greater current observed in Figure 3b. Nanocrystals of $CuGaO_2$ were also found to be much larger (width = 343 ± 71 nm; thickness = 40 ± 10 nm; aspect ratio = 8.6 ± 2.8) than $CuCrO_2$ and found to have significant particle stacking within the film structure (Figure S5), consistent with the literature.[26] Based on the delafossite crystal structure which only features copper surface terminations along the "sides" of the nanocrystals (e.g. (100) and (010) planes), the larger aspect ratio found for $CuGaO_2$ nanocrystals could further limit the percentage of the surface area terminated in electrochemically active copper sites. Notably, when the electrochemistry of a $CuGaO_2$ film was measured in 0.1 M $TBAClO_4$, the $Cu^{2+/+}$ redox

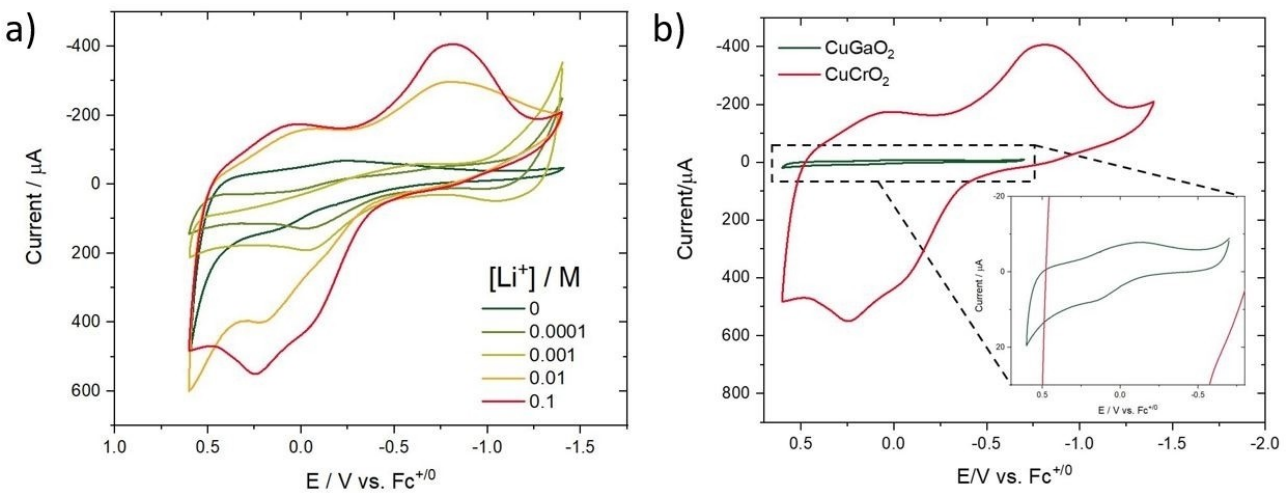

Figure 3. a) Comparison of CVs of the optimized $CuCrO_2$ thin film at 10 mV/s in electrolyte solutions containing mixtures of 0.1 M $LiClO_4$ and 0.1 M $TBAClO_4$ in MeCN. The total concentration was held constant at 0.1 M, however, the amount of Li + was varied across the series. b) CV of $CuGaO_2$ vs $CuCrO_2$ thin films in 0.1 M $LiClO_4$ in MeCN at 10 mV/s. (inset) A zoomed in image of the CV for $CuGaO_2$.

feature disappeared and the voltammogram was featureless until the potential exceeded 0.2 V vs $Fc^{+/0}$ where an irreversible oxidation was observed (Figure S6). This observation supports the idea that Li^+ dependent redox chemistry is associated with $Cu^{2+/+}$ redox chemistry.

Chronoamperometry experiments were conducted for $CuCrO_2$ films to quantitatively measure the increase in anodic and cathodic current with [Li^+]. Data were collected for a series of electrolyte solutions in 3 steps, with step 1 holding at −1.3 V vs $Fc^{+/0}$, followed by step 2 at 0.3 V, and returning to −1.3 V for step 3. These potentials were chosen so that a majority of the redox features could be captured without entering the irreversible oxidation observed near 0.5 V. Current versus time data is plotted in Figure S7 for each step and electrolyte condition. These data were then integrated to calculate the total charge passed as a function of time. Surprisingly, the measured charges for each step (Figures S8-S9 and Figure 4a) were found to be linear with $t^{1/2}$ at long times according to the Equation 1. This equation, known as the Anson equation, implies that faradaic current is being observed due to diffusion limited transfer of an electroactive species from solution to the electrode surface. However, in these experiments, the electrolyte is redox-inert, and this behavior must be explained by either diffusion of Li^+, TBA^+, or ClO_4^- to charge-balance redox changes within the $CuCrO_2$ film and/or diffusion of electrons/holes through the $CuCrO_2$ lattice associated with redox changes within the material. The linear slope of the diffusion region for the Anson plot can be used to calculate the diffusion coefficient (D_o), however, this requires knowledge of the concentration of electroactive species (C_o) and film surface area (A). Assuming the diffusion is the result of electrolyte ions, a concentration of 0.1 M, surface area of 343 cm^2, and electron transfer number of n = 1 results in diffusion coefficients reported in Table S3. These values were in the range of 10^{-14}–10^{-18}] cm^2/s and are remarkably low for typical ion diffusion through MeCN solvent. This could point to a more activation-controlled diffusion mechanism within the $CuCrO_2$ lattice.

What is more interesting about the Anson plots is that the intercepts from the linear fits, which report on the total adsorbed charge at the electrode surface (Q_{ads}), were found to increase and plateau at maximum values as [Li^+] increased (Table S4). The maximum $|Q_{ads}|$ value measured for each step was 8.4, 12, and 6.8 mC for steps 1, 2, and 3, respectively. The increase in Q_{ads} with [Li^+] for step 2 (0.3 V) is shown in Figure 4b and was found to fit well to a Langmuir binding isotherm using Equation 2, where Q_{max} is the maximum surface charge, and K is an equilibrium constant. Fitting to this equation implies an equilibrium between Li^+ ions and redox active surface sites of $CuCrO_2$. From this equation, an equilibrium constant K = 0.057 M^{-1} and maximum surface charge of Q_{max} = 15.5 mC were extracted.

$$Q = nFAC_o D_o^{1/2} t^{1/2} \pi^{-1/2} + Q_{ads} \quad (1)$$

$$Q_{ads} = \frac{K^* Q_{max}{}^* [Li^+]}{(1 + K^* [Li^+])} \quad (2)$$

The impact of small cations on the electrochemical features of metal oxides semiconductors has been well documented in the literature.[33–37] Most notably, cations such as Li^+ and H^+ have been observed to shift band edges by affecting the Helmholtz layer at the oxide surface to result in ~59 mV anodic shifts per order of magnitude increase in cation concentration. This has been most importantly observed for n-type TiO_2 electrodes and is exploited to lower the conduction band edge within dye-sensitized solar cells to allow for greater injection of excited-state electrons.[38–40] For p-type NiO, McCullough et al. have shown the valence band edge to likewise shift in a positive direction with increased charge density of the cation, where Al^{3+} was found to have the greatest shift.[40]

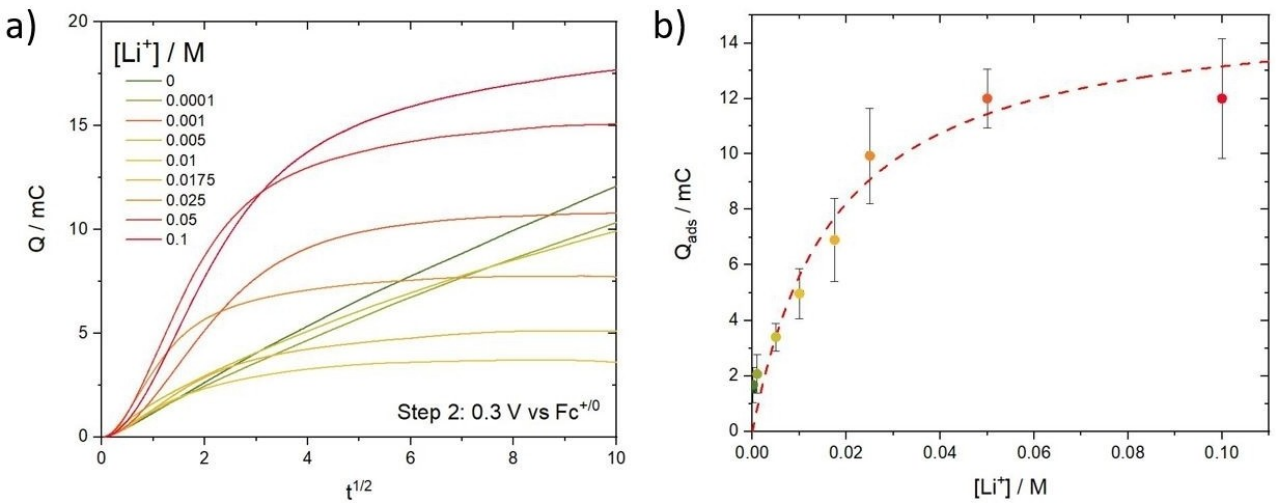

Figure 4. a) Anson plots constructed from integrated anodic chronoamperometry data using a series of electrolyte solutions with total concentration of 0.1 M and the [Li^+] adjusted from 0 M to 0.1 M. Each step was held at the fixed potential 0.3 V vs $Fc^{+/0}$ for 100 seconds. b) Q_{ads} plotted as a function of [Li^+] in electrolyte solution, fit to the Langmuir adsorption isotherm model.

In the present study, we believe that the feature observed at $E_{1/2} = 0.03$ V for 0 M [Li^+] is shifted positively to $E_{1/2} = 0.14$ V for 0.1 M [Li^+] based on the ability of Li^+ to affect the Helmholtz layer. We also believe the increase in current observed for this feature is likely due to the higher double layer capacitance available to Li^+ vs TBA^+, such that as TBA^+ ions are replaced with Li^+ in the electrolyte, a higher density of cations can form the double layer at the electrode surface.[41] Distinct from this observation is the new feature that emerged at $E_{1/2} = -0.43$ V for 0.1 M $LiClO_4$. The anodic wave for this feature was found at nearly the same potential for all [Li^+], but increased in magnitude as [Li^+] was increased. On the other hand, the cathodic wave shifted in a positive direction with increased [Li^+] while also increasing in magnitude.

These observations lead to our assignment of a Li-coupled redox feature in which Li^+ ions occupy specific sites at the $CuCrO_2$ surface generated by copper vacancy defects. A proposed redox reaction for this feature is shown in Equation 3. Here, the starting redox state of $CuCrO_2$ is dependent on the number of copper vacancies within the lattice (x) where every vacancy generates a corresponding Cu^{2+} ion to compensate charge. Reduction of Cu^{2+} to Cu^+ is accompanied by Li^+ insertion into the vacant site for charge balance. The positive shift in the cathodic peak could be explained by the fact that Li^+ is a reactant and thus increased [Li^+] could shift E_{pc} similar to proton-coupled electron transfer reactions.[42,43] Oxidation of Cu^+ back to Cu^{2+} therefore results in release of Li^+ ions from copper vacancy sites. Given the specific site occupation, TBA^+ ions are too large to occupy these positions and thus, the redox feature is not observed in 0.1 M $TBAClO_4$.

$$Cu^{+}_{1-2x}Cu^{2+}_{x}V_{Cu,x}Cr^{3+}O_2 + xLi^+ + xe^- \rightarrow Cu^{+}_{1-x}Li^{+}_{x}Cr^{3+}O_2 \qquad (3)$$

Fitting the surface charge data for the anodic step to a Langmuir binding isotherm implies that Li^+ ions bind to particular sites at the surface of $CuCrO_2$ nanocrystals with an equilibrium constant $K = 0.057\ M^{-1}$. Based on Equation 2, the measured surface charge should therefore be proportional to the number of copper vacancies. Based on a value of 4.0 ± 1.5% determined from ICP-MS for the same $CuCrO_2$ material published previously, we calculate that the expected charge would be 11 ± 5 mC.[30] The measured surfaces charges of 8.4 mC, 12 mC, and 6.8 mC for each chronoamperometric step are highly consistent with this estimate. It should be noted that the vacancy estimate from ICP-MS is a bulk value and not specific to surface copper vacancies. Therefore, the correlation between the expected charge for total vacancies and the measured charge could indicate that most if not all copper vacancies migrate to the surface of $CuCrO_2$ nanocrystals. Indeed, defect migration to surface sites is common in solid state materials and has been observed for $CuGaO_2$.[26]

It is also intriguing to think that Li^+ ions may be able to intercalate into the interior of the nanocrystal structure to occupy vacant sites in the bulk, given the structural similarities between $CuCrO_2$ and $LiCoO_2$. Both structures contain monovalent cations sandwiched between layers of edge-shared octahedra of trivalent cations. However, Li^+ is present in an octahedral coordination environment versus a linear coordination environment for Cu^+. To further explore this idea, we performed chronopotentiometric charge-discharge experiments on $CuCrO_2$ nanocrystalline films in MeCN with 0.1 M $LiClO_4$ electrolyte. The results from these experiments are shown in Figure 5 and summarized in Table S5-6.

At cycle 2, the charge observed at 0.6 V vs $Fc^{+/0}$ for $CuCrO_2$ was 15 mC, similar to that found in chronoamperometry experiments. Considering the dimensions of the $CuCrO_2$ film and assuming 50% porosity, 15 mC is equivalent to a 7.8 mA h g^{-1} storage capacity which is comparable to the theoretical 7.0 mA h g^{-1} with 4% copper vacancies present according to Equation 3. The experimental increase could be due to additional Li^+ incorporation into the film at a slightly higher potential. The discharge capacity was consistently much lower than the charge capacity for each cycle with a % cycling efficiency increasing from 83% to 91% over 10 cycles. By cycle 10, the charge capacity for $CuCrO_2$ in Li^+ decreased to 3.5 mA h g^{-1}. Conversely, the discharge capacity in Li^+ by cycle 10 was 3.2 mA h g^{-1}, respectively. Extended cycling of CV experiments revealed that the decrease in charge capacity was related to loss of the Li-coupled redox activity, as shown in Figure 6. Taken together, these data show there is irreversibility in the redox behavior, possibly due to incomplete removal of Li^+. The irreversibility could also be due to instability of the film in the form of degradation. Given that Cu^{2+} has a preferential square planar orientation, the increased Cu^{2+} concentration in linearly coordinated sites over the course of cycling could lead to increased strain on the structure, facilitating degradation of the film.

The pronounced increase in surface charge with increased Li^+ has important implications for $CuCrO_2$ nanocrystalline films within heterojunction solar cells. For example, many studies have focused on the impact of NiO surface defects on the performance of dye-sensitized solar cells.[7,8] The presence of such states has been associated with increased hole recombina-

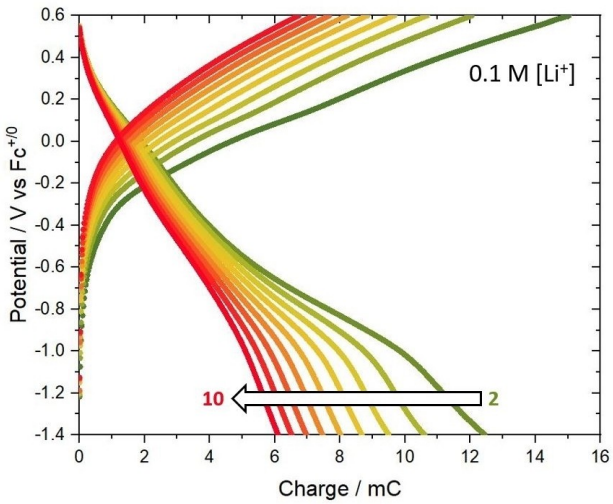

Figure 5. Cyclic charge-discharge chronopotentiograms for $CuCrO_2$ thin films held at 0.1 mA in 0.1 M $LiClO_4$. An arrow is shown to represent the degradation from cycle 2 (green) to cycle 10 (red).

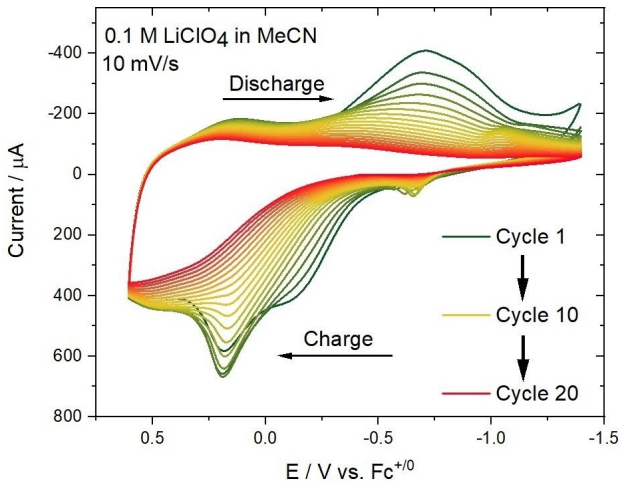

Figure 6. CV of $CuCrO_2$ film in 0.1 M $LiClO_4$ in MeCN at 10 mV/s scan rate over 20 consecutive cycles.

tion to molecular dyes and redox mediators, such that passivation of these states has resulted in improved photovoltages. Notably, passivation of surface defects also decreased photocurrent, suggesting that these surface states also have a role to play in accepting holes from excited-state molecules. The surface defects for $CuCrO_2$ were found to be activated by Li^+ and would be expected to behave in a similar fashion and thus limit the photovoltage of solar cell devices through faster recombination but increase photocurrent by expanding the density of states capable of accepting holes from excited-state molecules. Furthermore, it should be noted that common estimates for the valence band edge of $CuCrO_2$ and $CuGaO_2$ could be erroneously measured due to the onset of surface defects above the true valence band edge.

The ability of Li^+ to occupy copper vacancy sites within the delafossite lattice also has implications for electrochemical energy storage. Conventional Li-ion batteries with layered cathode structures utilize redox chemistry at the M^{3+} site accompanied by Li^+ intercalation. In the case of $CuCrO_2$, we have shown that redox chemistry is instead focused on the Cu^+ site; however, this is not to say that M^{3+} redox chemistry could not be accessed with other delafossite materials. Furthermore, research into the ability to control vacancy formation and ordering within the solid could enhance the reversibility and stability of Li^+ intercalation within delafossite materials.

Conclusion

Electrochemical characterization of nanocrystalline $CuCrO_2$ thin films was investigated in which a strong Li^+ dependence was observed via CV and chronoamperometry experiments. These observations resulted in a proposed redox reaction $Cu^+_{1-2x}Cu^{2+}_xV_{Cu,x}Cr^{3+}O_2 + xLi^+ + xe^- \rightarrow Cu^+_{1-x}Li^+_xCr^{3+}O_2$ in which Li^+ can occupy copper vacancy sites at the film surface. Due to the increased size of TBA^+, this redox reaction is not observed in the presence of electrolyte containing only TBA^+. Morphological variations among delafossite metal oxides was also explored and its impact on electrochemical characterization. When compared to its $CuGaO_2$ counterpart, $CuCrO_2$ films exhibited a much greater current in the cyclic voltammograms in 0.1 M $LiClO_4$ in MeCN which can be accounted for by the greater internal surface area of the $CuCrO_2$ films and smaller aspect ratio of nanocrystals. Finally, the redox reaction observed in the presence of Li^+ exhibits irreversibility, seen via chronopotentiometry experiments, and could be attributed to incomplete removal of Li^+ or degradation from strain caused by the linear coordination sites for Cu^{2+} cations. Future studies to improve the stability of these materials by means of controlling surface copper vacancy formation are needed in efforts to improve the cycling efficiency of the $CuCrO_2$. In addition, photoelectrochemical studies can be explored to understand how such surface defects impact hole recombination in heterojunction solar cells.

Experimental

Synthesis of $CuCrO_2$ and $CuGaO_2$ nanocrystals An optimized hydrothermal synthetic procedure was followed as previously reported for delafossite $CuCrO_2$ nanocrystals.[30] 20 mmol of chromium nitrate nonahydrate [$Cr(NO_3)_3 \cdot 9\,H_2O$] (Alfa Aesar, 98.5%) and 15 mmol copper nitrate hemipentahydrate [$Cu(NO_3)_2 \cdot 2.5\,H_2O$] (Alfa Aesar, 98%+) were added to 70 mL deionized H_2O (18 MΩ cm, Milli-Q) and stirred in an ice bath. After the precursors in water reached 5 °C, 7.03 g KOH (VWR Analytical) was added. The pH was measured before transferring the mixture into a 45 mL Teflon cup in order to ensure the solution pH > 13.

After transferring the mixture to the Teflon cup and sealing in an acid digestion bomb (Parr), the vessel was placed into a box furnace (Lindberg Blue M) and heated to 240 °C for 60 hours. After cooling to room temperature, the bomb was removed and the resulting mixture was centrifuged to separate the solid product from solution. The solid was dried and analyzed using powder X-ray diffraction before submerging in a 0.5 M NH_4OH (28 vol%, BDH) solution for 24 hours to allow for dissolution of impurities. The remaining product was rinsed with ethanol (Koptec, 200 Proof), ultrasonicated (Branson 150), and vortexed (VWR Analog Vortex Mixer) three times before allowing the product to dry in ethanol under a fume hood. The product was then placed in a vacuum oven (VWR) at 60 °C until further use.

$CuGaO_2$ was grown using a synthetic procedure previously reported.[26] 5 mmol of $Cu(NO_3)_2 \cdot 2.5\,H_2O$ (Alfa Aesar, 98%+) and 5 mmol $Ga(NO_3)_3 \cdot H_2O$ (Alfa Aesar, 99.99%) were dissolved in 15 mL deionized H_2O (18 MΩ cm, Milli-Q). The solution was chilled and stirred in an ice bath for 1 hour before adding 2.5 M KOH solution in 1 mL increments until the pH ~ 9. The final solution was transferred into a 45 mL Teflon-lined acid digestion bomb and placed into a box furnace at 190 °C for 24 hours. After cooling to room temperature, the solution was centrifuged and the solid product was separated from the aqueous solution and washed with ammonium hydroxide (NH_4OH, 28% vol %, BDH) to remove any Cu_2O impurities. The final product was washed with deionized water three times before a final acetone wash and dried in a vacuum oven.

Thin Film Electrode Fabrication Viscous pastes of $CuCrO_2$ and $CuGaO_2$ nanocrystals in ethanol solution were made using a 2:1 ratio of $CuCrO_2$:ethyl cellulose (Acros Organics, 10cP) where the final mixture contained 13 wt% $CuCrO_2$. Pastes were allowed to stir overnight to ensure homogeneity.

FTO glass (SnO_2:F, 15 Ω/cm^2, Hartford Glass, Inc.) was used as the conductive substrate and was prepared for deposition by sonication (Branson 3800) in a 0.1 M HCl (Gracs, 36%) ethanol solution for 20 minutes, followed by sonication in pure ethanol for 20 minutes. The glass was air dried, and CuCrO2 or CuGaO2 pastes were spin coated (Laurell WS650 MHz 23 NPPB) onto the FTO glass at 4,000 rpm for 30 seconds. After spin coating, the films were inserted into a tube furnace (Lindberg Blue M) at 350 °C for 30 minutes (296 mL/min flow rate) under flowing Ar (99.999%, Airgas). After allowing the films to cool to room temperature, they were placed in a desiccator until needed for electrochemical characterization.

Physical Characterization Powder X-ray diffraction (pXRD) data was collected using a Rigaku SmartLab X-Ray diffractometer with a Cu Kα source. XPS of the thin films was collected using a Physical Electronics (PHI) 5400 system with a monochromatic Al Kα source. High resolution scans of the O 1s, Cu 2p, and Cr 2p peaks were performed with a pass energy of 35.75 eV and a step size of 0.05 eV. The Casa XPS fitting software was used for all data analysis and fitting. Scanning electron microscopy (SEM) images were collected using a Hitachi S-4700. Transmission electron microscopy (TEM) images were collected using a Thermo Scientific Talos F200X. Thickness measurements of films were conducted using a Veeco Dektak 150 Stylus Surface Profilometer.

Surface area measurements of $CuCrO_2$ and $CuGaO_2$ thin films were performed using adsorption and desorption of a molecular dye. Films were first allowed to soak in a 300 μM P1 dye solution in acetonitrile for 24 hours (P1 = 4-(Bis- {4-[5-(2,2-dicyano-vinyl)-thiophene-2-yl]-phenyl}-amino)-benzoic acid, Dyenamo >95%). Films were then removed, rinsed with acetonitrile (MeCN), and then placed in a solution of 0.1 M KOH (BDH VWR Analytical) in 1:1 MeCN:H_2O (BDH:Milli-Q, 18 MΩ cm) to desorb all dye molecules from the oxide surface. The resulting solution was analyzed using an Agilent Cary 8454 UV-visible spectrophotometer to determine the amount of dye desorbed based on the solution volume and the extinction coefficient at 418 nm determined to be 42,000 M^{-1} cm^{-1} in 0.1 M KOH 1:1 MeCN:H_2O solution.[31] An estimated molecular footprint of the P1 dye (1.1×10^{10} cm^2 mol^{-1}) was then used to calculated the approximate surface area of $CuCrO_2$ and $CuGaO_2$ films. It should be noted that these surface areas are rough estimates which assumes the P1 dye does not aggregate. If aggregation were to occur, the estimation of surface area would be treated as a lower limit.

Electrochemical Characterization A Gamry 1010E potentiostat was used to conduct all electrochemical experiments with a 3-electrode electrochemical cell where the reference was an aqueous Ag/AgCl electrode (satd. KCl; BASi), the counter electrode was platinum mesh (BASi), and the working electrode was $CuCrO_2$ or $CuGaO_2$ thin films deposited on FTO glass. Cyclic voltammetry of an external ferrocene standard in acetonitrile with 0.1 M $LiClO_4$ electrolyte was performed before and after every experiment to ensure no potential drift was observed in the reference electrode. 0.1 M electrolyte solutions in MeCN containing $LiClO_4$ (99.99%, Millipore Sigma) and/or $TBAClO_4$ (BTC, 2537-36-2) were used to conduct all experiments. Nitrogen was used to purge the electrolyte solution before and during each experiment.

Acknowledgements

The authors thank Auburn University and the National Science Foundation (NSF-DMR-1809847) for supporting this research. pXRD data collection was performed on a Rigaku SmartLab diffractometer obtained through support from the National Science Foundation Major Research Instrumentation program (NSF-DMR-2018794). The authors thank Dr. Amar Kumbhar for TEM data collection at the CHANL facility located at the University of North Carolina at Chapel Hill, and Dr. Robert Jackson for help collecting profilometry measurements at Auburn University.

Conflict of Interest

The authors declare no conflict of interest.

Data Availability Statement

The data that support the findings of this study are available in the supplementary material of this article.

Keywords: $CuCrO_2$ · $CuGaO_2$ · delafossite · lithium intercalation · p-type metal oxide

[1] C. Zhen, T. Wu, R. Chen, L. Wang, G. Liu, H.-M. Cheng, *ACS Sustainable Chem. Eng.* **2019**, *7*, 4586–4618.
[2] T. Toyoda, Q. Shen, *J. Phys. Chem. Lett.* **2012**, *3*, 1885–1893.
[3] Y. Bai, I. Mora-Seró, F. De Angelis, J. Bisquert, P. Wang, *Chem. Rev.* **2014**, *114*, 10095–10130.
[4] E. Ramasamy, J. Lee, *J. Phys. Chem. C* **2010**, *114*, 22032–22037.
[5] J. A. Anta, E. Guillén, R. Tena-Zaera, *J. Phys. Chem. C* **2012**, *116*, 11413–11425.
[6] J. Huang, Z. Yin, Q. Zheng, *Energy Environ. Sci.* **2011**, *4*, 3861–3877.
[7] J. He, H. Lindström, A. Hagfeldt, S.-E. Lindquist, *J. Phys. Chem. B* **1999**, *103*, 8940–8943.
[8] L. Hu, J. Peng, W. Wang, Z. Xia, J. Yuan, J. Lu, X. Huang, W. Ma, H. Song, W. Chen, Y.-B. Cheng, J. Tang, *ACS Photonics* **2014**, *1*, 547–553.
[9] M. Yu, G. Natu, Z. Ji, Y. Wu, *J. Phys. Chem. Lett.* **2012**, *3*, 1074–1078.
[10] H. Zhang, H. Wang, W. Chen, A. K.-Y. Jen, *Adv. Mater.* **2017**, *29*, 1604984.
[11] S. Powar, D. Xiong, T. Daeneke, M. T. Ma, A. Gupta, G. Lee, S. Makuta, Y. Tachibana, W. Chen, L. Spiccia, Y.-B. Cheng, G. Götz, P. Bäuerle, U. Bach, *J. Phys. Chem. C* **2014**, *118*, 16375–16379.
[12] A. Hagfeldt, G. Boschloo, L. Sun, L. Kloo, H. Pettersson, *Chem. Rev.* **2010**, *110*, 6595–6663.
[13] B. O'Regan, M. Grätzel, *Nature* **1991**, *353*, 737–740.
[14] M. Yu, T. I. Draskovic, Y. Wu, *Phys. Chem. Chem. Phys.* **2014**, *16*, 5026–5033.
[15] Z. Xu, D. Xiong, H. Wang, W. Zhang, X. Zeng, L. Ming, W. Chen, X. Xu, J. Cui, M. Wang, S. Powar, U. Bach, Y.-B. Cheng, *J. Mater. Chem. A* **2014**, *2*, 2968–2976.
[16] F. Odobel, Y. Pellegrin, *J. Phys. Chem. Lett.* **2013**, *4*, 2551–2564.
[17] C. E. Creissen, J. Warnan, E. Reisner, *Chem. Sci.* **2018**, *9*, 1439–1447.
[18] J. Wang, V. Ibarra, D. Barrera, L. Xu, Y.-J. Lee, J. W. P. Hsu, *J. Phys. Chem. Lett.* **2015**, *6*, 1071–1075.
[19] J. Wang, Y.-J. Lee, J. W. P. Hsu, *J. Mater. Chem. C* **2016**, *4*, 3607–3613.
[20] K. Ueda, T. Hase, H. Yanagi, H. Kawazoe, H. Hosono, H. Ohta, M. Orita, M. Hirano, *J. Appl. Phys.* **2001**, *89*, 1790–1793.
[21] J. Tate, H. L. Ju, J. C. Moon, A. Zakutayev, A. P. Richard, J. Russell, D. H. McIntyre *Phys. Rev. B* **2009**, *80*, 165206.
[22] G. Hautier, A. Miglio, G. Ceder, G.-M. Rignanese, X. Gonze, *Nat. Commun.* **2013**, *4*, 2292.
[23] R. Gillen, J. Robertson, *Phys. Rev. B* **2011**, *84*, 035125.
[24] F. A. Benko, F. P. Koffyberg, *Mater. Res. Bull.* **1986**, *21*, 753–757.
[25] F. A. Benko, F. P. Koffyberg, *Phys. Status Solidi A* **1986**, *94*, 231–234.
[26] A. R. C. Bredar, M. D. Blanchet, R. B. Comes, B. H. Farnum, *ACS Appl. Mater. Interfaces* **2019**, *2*, 19–28.
[27] C. J. Flynn, S. M. McCullough, E. Oh, L. Li, C. C. Mercado, B. H. Farnum, W. Li, C. L. Donley, W. You, A. J. Nozik, J. R. McBride, T. J. Meyer, Y. Kanai, J. F. Cahoon, *ACS Appl. Mater. Interfaces* **2016**, *8*, 4754–4761.

[28] C. J. Flynn, S. M. McCullough, L. Li, C. L. Donley, Y. Kanai, J. F. Cahoon, *J. Phys. Chem. C* **2016**, *120*, 16568–16576.
[29] L. Tian, R. Tyburski, C. Wen, R. Sun, M. Abdellah, J. Huang, L. D'Amario, G. Boschloo, L. Hammarström, H. Tian, *J. Am. Chem. Soc.* **2020**, *142*, 18668–18678.
[30] A. L. Chown, B. H. Farnum, *Inorg. Chem.* **2022**, *61*, 8349–8355.
[31] A. R. C. Bredar, PhD thesis, Auburn University (USA) **2021**.
[32] R.-D. Zhao, Y.-M. Zhang, Q.-L. Liu, Z.-Y. Zhao, *Inorg. Chem.* **2020**, *59*, 16679–16689.
[33] M. T. Greiner, L. Chai, M. G. Helander, W.-M. Tang, Z.-H. Lu, *Adv. Funct. Mater.* **2012**, *22*, 4557–4568.
[34] G. Natu, P. Hasin, Z. Huang, Z. Ji, M. He, Y. Wu, *ACS Appl. Mater. Interfaces* **2012**, *4*, 5922–5929.
[35] B. Enright, G. Redmond, D. Fitzmaurice, *J. Phys. Chem.* **1994**, *98*, 6195–6200.
[36] G. Redmond, D. Fitzmaurice, *J. Phys. Chem.* **1993**, *97*, 1426–1430.
[37] G. Rothenberger, D. Fitzmaurice, M. Graetzel, *J. Phys. Chem.* **1992**, *96*, 5983–5986.
[38] N. G. Park, S. H. Jang, G. J. Kim, *Bull. Korean Chem. Soc.* **2000**, *21*, 1047–1048.
[39] S. Wu, H. Han, Q. Tai, J. Zhang, S. Xu, C. Zhou, Y. Yang, H. Hu, B. Chen, B. Sebo, X.-Z. Zhao, *Nanotechnology* **2008**, *19*, 215704.
[40] S. M. McCullough, J. M. Evans, T. Moot, A. D. Taggart, L. Troian-Gautier, J. F. Cahoon, *ACS Appl. Mater. Interfaces* **2020**, *3*, 1496–1505.
[41] M. Dunwell, Y. Yan, B. Xu, *Curr. Opin. Chem. Eng.* **2018**, *20*, 151–158.
[42] C. A. Kelly, F. Farzad, D. W. Thompson, J. M. Stipkala, G. J. Meyer, *Langmuir* **1999**, *15*, 7047–7054.
[43] W. Song, H. Luo, K. Hanson, J. J. Concepcion, M. K. Brennaman, T. J. Meyer, *Energy Environ. Sci.* **2013**, *6*, 1240–1248.

Manuscript received: August 3, 2022
Revised manuscript received: October 4, 2022

RESEARCH ARTICLE

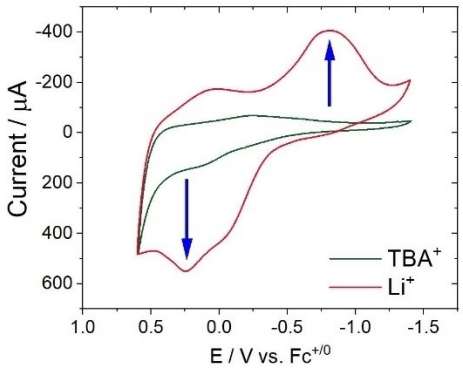

*A. L. Chown, H. Yeasmin, R. Paudel, Prof. R. B. Comes, Prof. B. H. Farnum**

Electrochemistry of $CuCrO_2$: The electrochemistry of $CuCrO_2$ nanocrystals shows a pronounced dependence on Li^+ cations, assigned to lithium coupled redox chemistry at copper vacancy surface defects sites. Such defect sites could play important roles in interfacial electron transfer reactions within solar cell devices.